Particles I

Access the latest eBook →

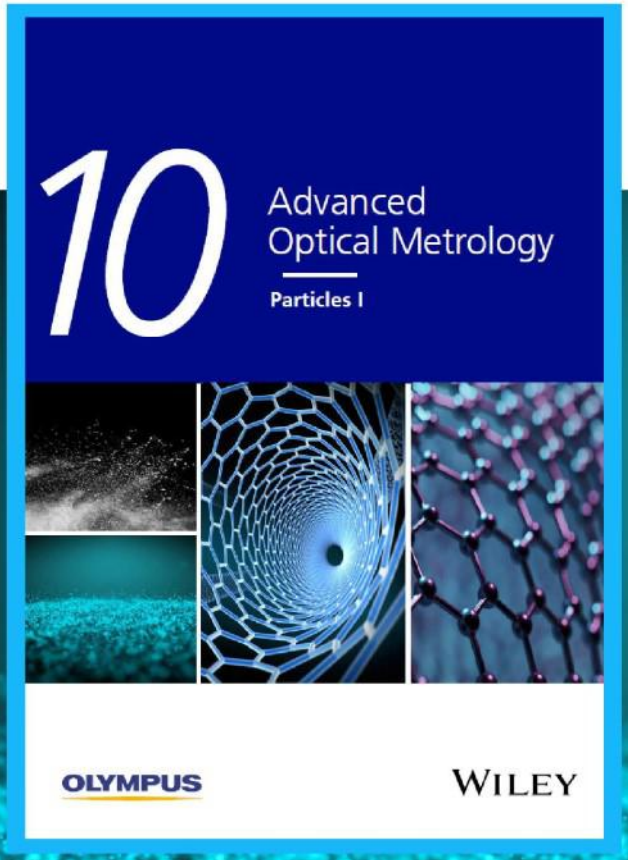

Particles: Unique Properties, Uncountable Applications

Read the latest eBook and better your knowledge with highlights from the recent studies on the design and characterization of micro- and nanoparticles for different application areas.

Access Now

This eBook is sponsored by

OLYMPUS

WILEY

ADVANCED FUNCTIONAL MATERIALS
www.afm-journal.de

Giant Nonlinear Optical Absorption of Ion-Intercalated Tin Disulfide Associated with Abundant In-Gap Defects

Mengjuan Diao, Hui Li, Xiangyun Gao, Ruipeng Hou, Qian Cheng, Zhiyang Yu, Zhipeng Huang, and Chi Zhang**

Herein it is reported that electrochemical ion-intercalation is a convenient and effective strategy toward materials with giant nonlinear optical (NLO) absorption. Alkali-metal ions (i.e., Li^+, Na^+, K^+) are electrochemically intercalated into SnS_2 nanosheets. All ion-intercalated samples exhibit remarkably enhanced optical nonlinearity compared with an untreated sample, and Li-intercalated SnS_2 ($Li_{0.952}Sn^{II}_{0.398}Sn^{IV}_{0.563}S_2$) possesses optimized strong NLO performance. $Li_{0.952}Sn^{II}_{0.398}Sn^{IV}_{0.563}S_2$ exhibits strong saturable absorption, and the corresponding nonlinear absorption coefficient (β_{eff}) is -1.7×10^4 cm GW^{-1} for the laser excitation at 515 nm. $Li_{0.952}Sn^{II}_{0.398}Sn^{IV}_{0.563}S_2$ shows prominent reverse saturable absorption with the laser excitation at 800 nm (β_{eff}: 2.8×10^4 cm GW^{-1}) and 1030 nm (β_{eff}: 1.4×10^4 cm GW^{-1}). All β_{eff} values are larger than most of the reported inorganic NLO materials at corresponding wavelengths. The optical limiting threshold of $Li_{0.952}Sn^{II}_{0.398}Sn^{IV}_{0.563}S_2$ is 8×10^{-4} J cm^{-2}, two orders of magnitude smaller (better) than the benchmark composite (e.g., SWNT-NH-TPP). Ion intercalation introduces abundant in-gap defects. The excitation of electrons in in-gap states to conduction band intensifies the Pauli-blocking effect and therefore promotes the saturable absorption under the 515 nm laser excitation, while the in-gap defect states acting as effective excitation pathway facilitate excited-state absorption for 800 and 1030 nm laser.

1. Introduction

Nonlinear optical (NLO) process is induced when the intense laser interacts with materials, which correlates the fundamental optical process with a series of civil, industrial, and military applications by using the ultrafast and superstrong laser (e.g., pulse laser generation,[1] nonlinear optical image,[2] optical sensor/human eyes protection,[3] optical modulating/switching[4]). Developing high-performance NLO materials is scientifically interesting and technically important. Among many candidate materials, two-dimensional (2D) materials are very attractive because of their ultrafast carrier dynamics, wideband absorption, strong excitonic effect, quantum confinement, etc. The NLO properties of a large number of 2D materials have been studied, e.g., graphene,[5,6] graphdiyne,[7,8] black phosphorus,[9,10] metal chalcogenides,[11–14] MXenes,[15,16] 2D hybrid Ruddlesden-Popper-type halide perovskites (RPPs).[17,18] Although various approaches have been devoted to developing high-performance 2D materials (e.g., the synthesis of new 2D materials, [5–13,15–18] the construction of heterojunction with inorganic or organic semiconductors,[6,19–21] the control of the thickness of 2D materials,[14,22] the doping of 2D materials[23]), the further device application of 2D NLO materials remains being hindered by their disadvantages in addition to the weak performance, e.g., the low damage threshold[24] and zero bandgap[25] of graphene, the poor air stability of black phosphorus[26] and organic–inorganic hybrid halide perovskite,[27] and in particular the low-yield synthesis (e.g., chemical vapor deposition,[14] mechanical exfoliation[17]) of high-performance materials. Accordingly, an effective strategy for the development of high-performance NLO materials is highly desirable. The large ratio of surface atoms suggests that the performance of 2D semiconductors is susceptible to defects, which has been implied by the fact that even the same 2D material synthesized by different approaches or different researchers (e.g., MoS_2,[12,28] $Ti_3C_2T_x$,[29,30] black phosphorus,[9,10] RPPs[17]) might show different NLO properties. The contribution of defects to NLO process remains unclear.[17,31–33] For example, defects would prevent efficient excitonic interactions in 2D hybrid RPPs and downgrade its NLO properties,[17] which is in sharp contrast to the defect-related resonance absorption in indium tin oxide that led to prominent saturable absorption.[31] These reports manifest that defect control is of the utmost

M. Diao, H. Li, X. Gao, R. Hou, Z. Huang, C. Zhang
School of Chemical Science and Engineering
Tongji University
Shanghai 200092, P. R. China
E-mail: zphuang@tongji.edu.cn; chizhang@tongji.edu.cn
Q. Cheng, Z. Huang
Shanghai Research Institute for Intelligent Autonomous Systems
Shanghai 201210, P. R. China
Z. Yu
State Key Laboratory of Photocatalysis on Energy and Environment
College of Chemistry
Fuzhou University
Fuzhou 350002, P. R. China
The ORCID identification number(s) for the author(s) of this article can be found under https://doi.org/10.1002/adfm.202106930.

DOI: 10.1002/adfm.202106930

importance for the development of high-performance NLO materials, while the related study into defect-related NLO performance is however unexplored to date due to the absence of an effective defect-modulation pathway.

As a striking feature of 2D materials, the large inter-layer space associated with the weak van der Waals interaction between layers in 2D materials is beneficial for electrochemical ion intercalation. Electrochemical ion intercalation can provide various unique possibilities for the defect modulation and may afford a novel and effective strategy for developing high-performance NLO materials. Firstly, external intercalated ions can be considered as chemical impurities of the host materials, and the ion intercalation leads to the lattice imperfection (expansion). These two factors would introduce defect states to the host materials. Secondly, the number of intercalation ions can be well controlled by electrochemical charging or discharging, making the introduction of defects highly controllable and reversible. Thirdly, the electrochemical ion intercalation can be considered as electrochemical doping, which may possess advantages in achieving high doping level and/or non-equilibrium states that are usually hard to be implemented by ordinary chemical doping. However, although electrochemical ion intercalation has been successfully used in 2D-material synthesis,[34,35] energy storage,[36–39] and electronic/magnetic devices (e.g., synaptic transistor,[40] superconductor,[41] thermoelectrics,[42] ferromagnetism[43]), there is no report to date regarding the NLO performance of ion-intercalated 2D materials.

In this study, we report that electrochemical ion intercalation is a convenient and effective strategy toward NLO materials with giant NLO absorption. Alkali-metal ions (i.e., Li^+, Na^+, K^+) have been electrochemically intercalated into SnS_2 nanosheets, all resulting in remarkably promoted NLO absorption performance. In particular, resultant $Li_{0.952}Sn^{II}_{0.398}Sn^{IV}_{0.563}S_2$ possesses strong saturable absorption under laser excitation at 515 nm (nonlinear absorption coefficient, β_{eff}: -1.7×10^4 cm GW^{-1}). The $Li_{0.952}Sn^{II}_{0.398}Sn^{IV}_{0.563}S_2$ exhibits prominent reverse saturable absorption under laser excitation at 800 nm (β_{eff}: 2.8×10^4 cm GW^{-1}) and 1030 nm (β_{eff}: 1.4×10^4 cm GW^{-1}). All β_{eff} values are larger than most of the reported inorganic NLO materials. The optical limiting threshold is 8×10^{-4} J cm^{-2}, two orders of magnitude smaller (better) than those of reported materials. The superb performance is associated with the introduction of abundant in-gap defect states via ion intercalation. The defect states intensify Pauli blocking under laser excitation at 515 nm, and offer abundant excitation pathways facilitating the excited state absorption under laser excitation at 800 and 1030 nm. Our study not only demonstrates ion-intercalated materials as a new family of high-performance NLO materials, but also provides a new paradigm for constructing NLO materials with significantly enhanced performance by defect modulation.

2. Results and Discussion

Berndtite 2T SnS_2 was adopted as a host material, and Li^+, Na^+, K^+ were intercalated to SnS_2 nanosheets. As a 2D semiconductor, SnS_2 is considered as a promising anode material for Li^+ batteries and Na^+ batteries.[39,44] Meanwhile, SnS_2 has demonstrated its optoelectronic application such as fast photodetectors,[45] solar cells, thin-film transistors due to its appropriate semiconducting characteristics and good optical properties.[46,47] The atomic structure of SnS_2 was schematically illustrated in **Figure 1**a. The SnS_2 has a space group of $P\bar{3}m1$, and the atomic structure is composed of S-Sn-S layer stacking along the [001] direction. The adjacent layers are bonded by weak van der Waals force, and the distance between two adjacent layers is as large as 2.94 Å, providing large open channels for ion intercalation and diffusion. The theoretical calculation indicates that the alkaline atoms can be introduced to octahedral sites between S–S layers.[48] The ionic radius is 0.76 Å for Li^+, 1.02 Å for Na^+, and 1.38 Å for K^+.[49] Different ionic radii would result in different volume expansions of the host SnS_2, and would lead to different defect levels. Meanwhile, the number of defect states can be modulated by the number of intercalated ions, which can be conveniently implemented by electrochemical ion intercalation with different charging times.

In this study, we investigate the nonlinear response of SnS_2 intercalated with ions of different radii and the radius-dependent NLO response of ion-intercalated SnS_2 (Figure 1b). The fluorine-doped tin oxide (FTO) loaded with SnS_2 nanosheets was assembled into a transparent electrochemical cell, and the NLO response of the sample was measured in a typical open aperture *Z*-scan setup under different electrochemical potential (namely, different ion intercalation status).

Vertically aligned SnS_2 nanosheets on the FTO substrate were used in this study, and the synthesis can be found in our previous publication.[50] The SnS_2 nanosheets covered uniformly on FTO substrate. Scanning electron microscopy (SEM) image (Figure 1c) shows that the SnS_2 nanosheets are vertically aligned and have a crumpled surface. The inset of Figure 1c shows that the surface of SnS_2 nanosheets is smooth. The thickness of the films is ≈230 nm (Figure S1a in the Supporting Information). The typical thickness of SnS_2 nanosheets is ≈8 nm (Figure 1d). High magnification transmission electron microscopy (TEM) image (Figure 1e) presences clearly the layer structure. Figure 1f is the integrated line intensity profile corresponding to a region enclosed by rectangle in Figure 1e. It is indicated that the average interlayer distance of 0.59 nm, in good accordance with that between (001) plane of Berndtite 2T SnS_2. The nanosheets are composed of tiny grains (Figure 1g), and the grains have a lateral size of around 5 nm. The tiny plates are crystalline, with lattice fringes well-defined. Inset of Figure 1g shows an example of lattice fringes, which can be indexed to (101) plane ($d_{(101)}$ = 2.9 Å) and (110) plane ($d_{(110)}$ = 1.8 Å). The radial intensity profile of selected area electron diffraction (SAED) pattern (Figure S1b,c in the Supporting Information) confirms that the SnS_2 is crystallized in hexagonal structure (JCPDS No 23–0677).

In our experiment, the ion intercalation was implemented by potentiostatic experiment at the desired voltage. Typically, a voltage corresponding to the reductive peak in the cyclic voltammogram was applied to the sample (Figure S2 in the Supporting Information), and it is –1.1, –1.5, and –1.6 V for the intercalation of Li^+, Na^+, and K^+, respectively. Corresponding acetonitrile solution of metal hexafluorophosphate was used as electrolyte. The intercalation time is 2 min, and this duration is sufficiently

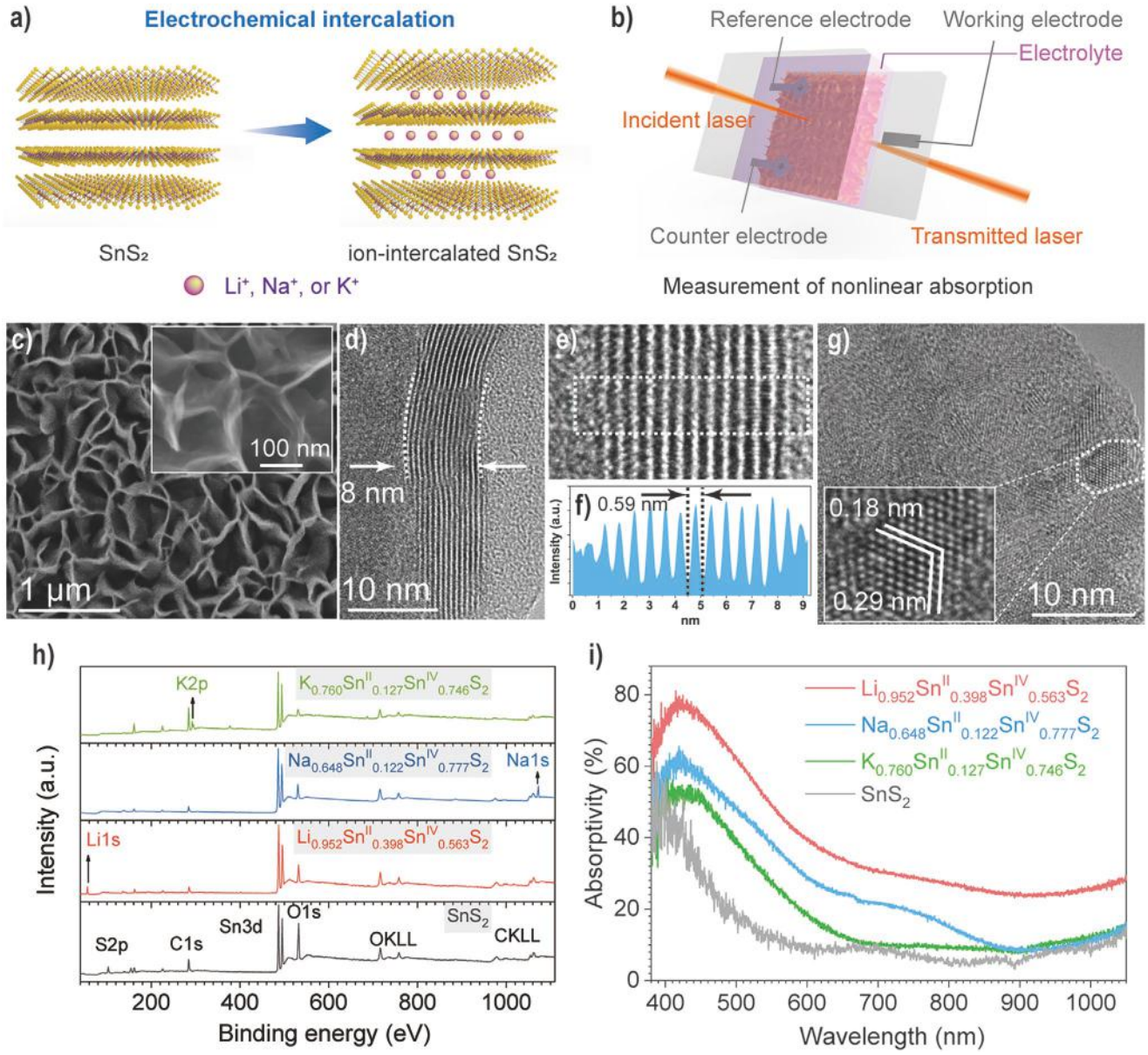

Figure 1. a) Schematic of the electrochemical ion intercalation of SnS_2. b) Schematic of a transparent electrochemical cell for the in-situ measurement of nonlinear transmittance. c) Plan-view SEM images of SnS_2 nanosheets. d) TEM image of a vertically aligned SnS_2 nanosheet. e) High resolution TEM image and f) corresponding line profile of a vertically aligned SnS_2 nanosheet. g) TEM image of a SnS_2 nanosheet. Inset of (g) shows the high resolution TEM image of a particle enclosed by broken lines in (g). h) Survey XPS spectra of SnS_2 and SnS_2 intercalated by different ions. i) Absorption spectra of SnS_2 and SnS_2 intercalated by different ions.

long to finish the ion intercalation or deintercalation. X-ray photoelectron spectroscopy (XPS) experiments confirm the presence of Li, Na, and K in the intercalated SnS_2 (Figure 1h), the atomic ratio of M (i.e., Li, Na, or K), Sn, and S derived from XPS experiments (Table S1 in the Supporting Information) suggests that the resultant compounds are $Li_{0.952}Sn^{II}_{0.398}Sn^{IV}_{0.563}S_2$, $Na_{0.648}Sn^{II}_{0.122}Sn^{IV}_{0.777}S_2$, and $K_{0.760}Sn^{II}_{0.127}Sn^{IV}_{0.746}S_2$. The ion intercalation can be described by the reaction: $xM^+ + SnS_2 + xe^- \rightarrow M_xSnS_2$, where M is Li, Na, or K and x ranges 0 to 1. On the other hand, the ion-intercalated samples can also be activated at opposite direction by applying a positive potential (a deintercalation process). The bandgap of SnS_2 can be modified by ion-intercalation, suggested by the gradual red shift of absorption edge with decreasing the radius of intercalation ions (Figure 1i).

The voltage is on during the Z-scan measurement. The normalized transmittance (T_{NL}) of the device was recorded at different positions (z), for which the focal point of the incident laser was defined as the zero position. Meanwhile, the $T_{NL}(z)$ of a blank device assembled by two bare FTO substrates indicates a negligible response (Figure S3 in the Supporting Information), confirming that all NLO responses discussed

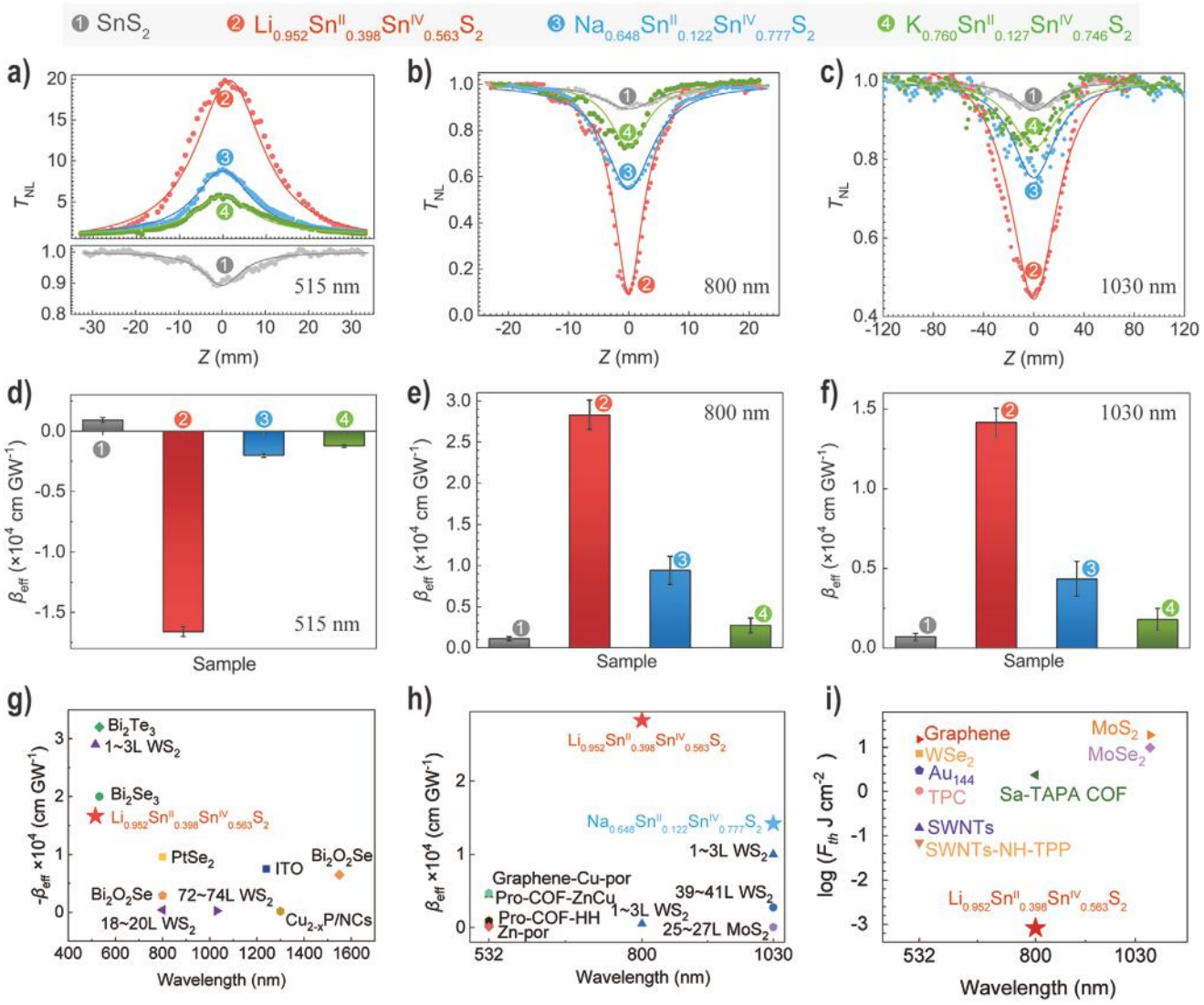

Figure 2. $T_{NL}(z)$ curves of SnS_2, $Li_{0.952}Sn^{II}_{0.398}Sn^{IV}_{0.563}S_2$, $Na_{0.648}Sn^{II}_{0.122}Sn^{IV}_{0.777}S_2$, $K_{0.760}Sn^{II}_{0.127}Sn^{IV}_{0.746}S_2$ with laser excitations at a) 515 nm, b) 800 nm, c) 1030 nm. The scatters are experimental data and the solid lines are fitting results. β_{eff} of SnS_2, $Li_{0.952}Sn^{II}_{0.398}Sn^{IV}_{0.563}S_2$, $Na_{0.648}Sn^{II}_{0.122}Sn^{IV}_{0.777}S_2$, $K_{0.760}Sn^{II}_{0.127}Sn^{IV}_{0.746}S_2$ with laser excitations at d) 515 nm, e) 800 nm, f) 1030 nm. The comparison of g) saturable absorption, h) reverse saturable absorption, and i) optical limiting threshold of $Li_{0.952}Sn^{II}_{0.398}Sn^{IV}_{0.563}S_2$ with representative NLO materials.

hereafter come exclusively from SnS_2 and ion-intercalated samples. **Figure 2**a is typical *Z*-scan curves of pristine SnS_2, $Li_{0.952}Sn^{II}_{0.398}Sn^{IV}_{0.563}S_2$, $Na_{0.648}Sn^{II}_{0.122}Sn^{IV}_{0.777}S_2$, and $K_{0.760}Sn^{II}_{0.127}Sn^{IV}_{0.746}S_2$ excited with 515 nm laser. With sample close to the focus (smaller *z*), the $T_{NL}(z)$ of SnS_2 decreases, suggesting that the $T_{NL}(z)$ decreases with increasing laser intensity and that the NLO response of pristine SnS_2 is reverse saturable absorption. The response switches dramatically after ions intercalation. For $Li_{0.952}Sn^{II}_{0.398}Sn^{IV}_{0.563}S_2$, $Na_{0.648}Sn^{II}_{0.122}Sn^{IV}_{0.777}S_2$, and $K_{0.760}Sn^{II}_{0.127}Sn^{IV}_{0.746}S_2$, a $T_{NL}(z)$ larger than 1 is obtained at the focus, and the $T_{NL}(z)$ is 20 for $Li_{0.952}Sn^{II}_{0.398}Sn^{IV}_{0.563}S_2$, 9 for $Na_{0.648}Sn^{II}_{0.122}Sn^{IV}_{0.777}S_2$, and 6 for $K_{0.760}Sn^{II}_{0.127}Sn^{IV}_{0.746}S_2$, respectively. It shows that all ion intercalated SnS_2 samples exhibit a strong saturable absorption, namely, larger laser intensity (at smaller *z* position) results in larger T_{NL}.

The β_{eff} of samples were extracted from $T_{NL}(z)$ curves by data fitting. For each sample, three $T_{NL}(z)$ curves were measured at different regions (Figure S4 in the Supporting Information), and the average values of β_{eff} and their standard deviations are plotted in Figure 2d. With laser excitation at 515 nm, the β_{eff} is $(9.0 \pm 2.0) \times 10^2$ cm GW^{-1} for the pristine SnS_2, $(-1.7 \pm 0.1) \times 10^4$ cm GW^{-1} for the $Li_{0.952}Sn^{II}_{0.398}Sn^{IV}_{0.563}S_2$, $(-2.0 \pm 0.2) \times 10^3$ cm GW^{-1} for the $Na_{0.648}Sn^{II}_{0.122}Sn^{IV}_{0.777}S_2$, and $(-1.2 \pm 0.1) \times 10^3$ cm GW^{-1} for the $K_{0.760}Sn^{II}_{0.127}Sn^{IV}_{0.746}S_2$.

The NLO response of SnS_2 can also be activated by ion intercalation for laser excitation of 800 and 1030 nm. Figure 2b,c,e,f shows the $T_{NL}(z)$ curves and corresponding β_{eff} of various samples. Both pristine SnS_2 and ion-intercalated SnS_2 show reverse saturable absorption for 800 and 1030 nm laser, and the reverse saturable absorption of ion-intercalated SnS_2 is much more pronounced than pristine SnS_2. At 800 nm the β_{eff} is

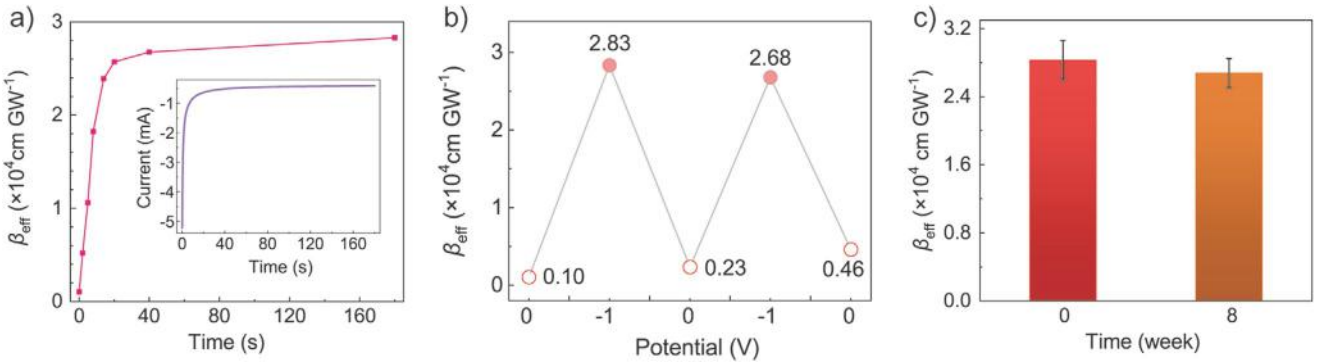

Figure 3. a) Variation of β_{eff} with the intercalation time of Li^+ into SnS_2. b) β_{eff} of SnS_2 corresponding to cycles of Li-intercalation and de-intercalation. c) β_{eff} of fresh prepared $Li_{0.952}Sn^{II}_{0.398}Sn^{IV}_{0.563}S_2$ and $Li_{0.952}Sn^{II}_{0.398}Sn^{IV}_{0.563}S_2$ stored in ambient atmosphere for 8 weeks. Inset of (a) shows a typical current-time curve corresponding to the ion intercalation of Li^+ in to SnS_2 with the potential of –1.1 V.

$(1.1 \pm 0.2) \times 10^3$ cm GW^{-1} for pristine SnS_2, $(2.8 \pm 0.2) \times 10^4$ cm GW^{-1} for $Li_{0.952}Sn^{II}_{0.398}Sn^{IV}_{0.563}S_2$, $(9.4 \pm 1.7) \times 10^3$ cm GW^{-1} for $Na_{0.648}Sn^{II}_{0.122}Sn^{IV}_{0.777}S_2$, and $(2.7 \pm 0.9) \times 10^3$ cm GW^{-1} for $K_{0.760}Sn^{II}_{0.127}Sn^{IV}_{0.746}S_2$. The enhancement factor (EF), defined as the ratio between the β_{eff} of ion-intercalated sample to the pristine sample, is as large as 26 for $Li_{0.952}Sn^{II}_{0.398}Sn^{IV}_{0.563}S_2$, 8.5 for $Na_{0.648}Sn^{II}_{0.122}Sn^{IV}_{0.777}S_2$, and 2.5 for $K_{0.760}Sn^{II}_{0.127}Sn^{IV}_{0.746}S_2$. It will be discussed later that with laser excitation at 1030 nm the reverse saturable absorption of SnS_2 contains the contribution of both two-photon absorption (2PA) and three-photon absorption (3PA), while only 2PA process occurs in the ion-intercalated SnS_2 nanosheets. The β_{eff} of SnS_2 is $(0.6 \pm 0.2) \times 10^3$ cm GW^{-1}, and the γ_{eff} is $(0.4 \pm 0.3) \times 10^3$ cm^3 GW^{-2}. On the other hand, the β_{eff} is $(1.4 \pm 0.1) \times 10^4$ cm GW^{-1} for $Li_{0.952}Sn^{II}_{0.398}Sn^{IV}_{0.563}S_2$, $(4.4 \pm 1.1) \times 10^3$ cm GW^{-1} for $Na_{0.648}Sn^{II}_{0.122}Sn^{IV}_{0.777}S_2$, and $(1.8 \pm 0.7) \times 10^3$ cm GW^{-1} for $K_{0.760}Sn^{II}_{0.127}Sn^{IV}_{0.746}S_2$, all values being much larger than that of pristine SnS_2.

It is shown that in a broad wavelength range (515–1030 nm), the optical nonlinearity of SnS_2 can be dramatically switched or modulated by ion intercalations. Meanwhile, the modulation effect correlates strongly with the atomic number of intercalation elements. An intercalation atom with a smaller atomic number results in a better performance of ion-intercalated SnS_2. The $Li_{0.952}Sn^{II}_{0.398}Sn^{IV}_{0.563}S_2$ has the best performance at all wavelengths. The nonlinear absorption response of $Li_{0.952}Sn^{II}_{0.398}Sn^{IV}_{0.563}S_2$ is also better than most of reported inorganic semiconductors. With laser excitation at 515 nm, the β_{eff} of $Li_{0.952}Sn^{II}_{0.398}Sn^{IV}_{0.563}S_2$ $(-1.7 \pm 0.1) \times 10^4$ cm GW^{-1}) is only smaller than that of 1–3 layer WS_2 (-2.9×10^4 cm GW^{-1}), Bi_2Se_3 (-2.0×10^4 cm GW^{-1}), and Bi_2Te_3 (-3.2×10^4 cm GW^{-1}), while larger than all other inorganic semiconductors (Figure 2g and Table S2 in the Supporting Information). Among materials showing reverse saturable absorption, the $Li_{0.952}Sn^{II}_{0.398}Sn^{IV}_{0.563}S_2$ exhibit the largest β_{eff} (Figure 2h and Table S3 in the Supporting Information). The optical limiting threshold (F_{th}) can be derived from the *Z*-scan curve where the T_{NL} dropped to 0.5. The F_{th} is as small as 8×10^{-4} J cm^{-2} for $Li_{0.952}Sn^{II}_{0.398}Sn^{IV}_{0.563}S_2$, the value is approximately two orders of magnitude smaller (better) than that of bench-mark composite (SWNT-NH-TPP[51]) (Figure 2i and Table S4 in the Supporting Information). Given the easy implementation of ion intercalation and the abundant candidates of host materials, ion intercalation would be a convenient and effective approach to promoting the NLO performance of materials.

Electrochemical ion intercalation is a continuous process, suggesting that the NLO response of SnS_2 can be continuously modulated. **Figure 3**a shows a typical current (*i*) – time (*t*) curve corresponding to the potentiostatic Li intercalation of SnS_2, and the β_{eff} of Li_xSnS_2 charged for different times. The β_{eff} was measured at 800 nm, and corresponding *Z*-scan curves can be found in Figure S5 in the Supporting Information. It is shown that the charging current decreases gradually with time, and longer than 40 seconds the variation of current is negligible. The variation of β_{eff} with time has the same trend as current, the β_{eff} changes from 1.1×10^3 to 2.7×10^4 cm GW^{-1} in 40 s. The time-dependent activation of Li_xSnS_2 can also be found for laser excitation at 515 and 1030 nm (Figure S6 in the Supporting Information). Therefore, electrochemical ion-intercalation is a convenient approach to modulating the optical nonlinearity of SnS_2, and the desired performance can be obtained by only changing the charging time.

The optical nonlinearity can be activated at opposite direction by the electrochemical deintercalation process (Figure S7 in the Supporting Information). Applied with a voltage of 1.5 V for 8 min, the β_{eff} of $Li_{0.952}Sn^{II}_{0.398}Sn^{IV}_{0.563}S_2$ was dramatically reduced to 0.23×10^4 cm GW^{-1} (Figure 3b), suggesting that the superb performance of $Li_{0.952}Sn^{II}_{0.398}Sn^{IV}_{0.563}S_2$ correlates strongly with Li^+ intercalation. The intercalation and deintercalation can be carried out repeatedly, suggesting that ion-intercalation/deintercalation can be potentially used to dynamically modulate the NLO performance. Figure 3b shows that although the β_{eff} of $Li_{0.952}Sn^{II}_{0.398}Sn^{IV}_{0.563}S_2$ is nearly the same for different intercalation/deintercalation number, the β_{eff} of ion-deintercalated SnS_2 increase, with the sample subjected to two cycles of intercalation/deintercalation has a β_{eff} 4.0 times of the pristine SnS_2. It will be discussed later that this performance enhancement can be ascribed to the structural defects induced by repeatedly intercalation/deintercalation.

The $Li_{0.952}Sn^{II}_{0.398}Sn^{IV}_{0.563}S_2$ sample was dissembled from the electrochemical cell, and kept in the ambient atmosphere for 8 weeks. Corresponding *Z*-scan (Figure S8 in the Supporting Information) shows that the β_{eff} of $Li_{0.952}Sn^{II}_{0.398}Sn^{IV}_{0.563}S_2$ is 2.68×10^4 cm GW^{-1} (Figure 3c), 94% of to the sample with bias

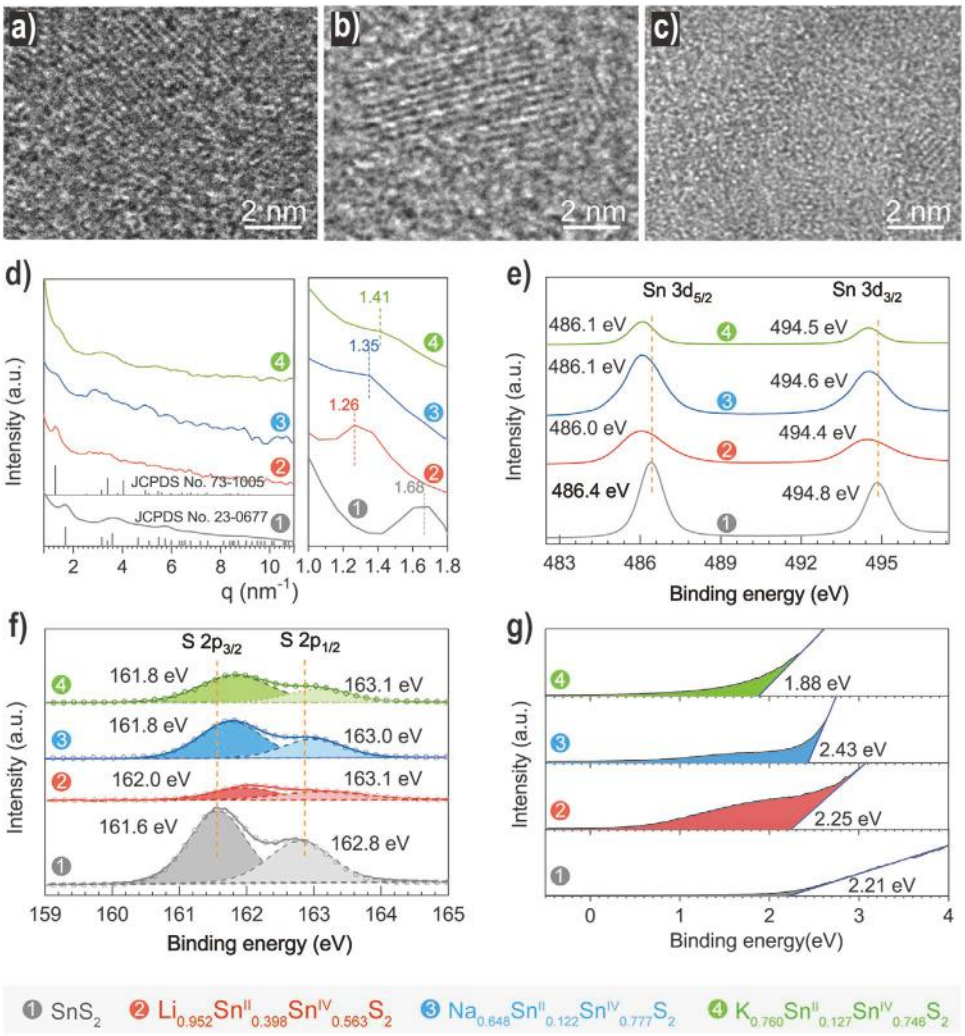

Figure 4. TEM images of a) $Li_{0.952}Sn^{II}_{0.398}Sn^{IV}_{0.563}S_2$, b) $Na_{0.648}Sn^{II}_{0.122}Sn^{IV}_{0.777}S_2$, and c) $K_{0.760}Sn^{II}_{0.127}Sn^{IV}_{0.746}S_2$. d) Radial intensity profiles of diffraction patterns of SnS_2 and Li-intercalated samples. e) Sn 3d window and f) S 2p window of the XPS spectra of SnS_2 and ion-intercalted SnS_2. g) UPS spectra of SnS_2 and ion-intercalated SnS_2.

on. It is suggested that the ion-intercalated SnS_2 is sufficiently stable in air, and can act as high-performance off-line NLO materials.

To reveal the origin of performance enhancement after ion intercalation, the morphology, structure, and chemical state of pristine SnS_2 and ion-intercalated SnS_2 were monitored. The morphology of samples after ion intercalation is revealed by SEM images (Figure S9 in the Supporting Information). After ions intercalation, the porous framework of pristine SnS_2 was maintained, while the nanosheets became much rougher. TEM images of ion-intercalated samples were shown in panels a to c of **Figure 4** for $Li_{0.952}Sn^{II}_{0.398}Sn^{IV}_{0.563}S_2$, $Na_{0.648}Sn^{II}_{0.122}Sn^{IV}_{0.777}S_2$, and $K_{0.760}Sn^{II}_{0.127}Sn^{IV}_{0.746}S_2$, respectively. In contrast to pristine SnS_2 who shows well-defined lattice fringes, the lattice fringes are hard to identify in ion-intercalated SnS_2. Typically, a region with short-range order has a size smaller than 2 nm for $Li_{0.952}Sn^{II}_{0.398}Sn^{IV}_{0.563}S_2$ and $Na_{0.648}Sn^{II}_{0.122}Sn^{IV}_{0.777}S_2$, and no long-range ordering can be found for $K_{0.760}Sn^{II}_{0.127}Sn^{IV}_{0.746}S_2$, suggesting that the significant degradation of crystallinity because of ion intercalation. The microstructure of ion-intercalated SnS_2 was derived from the SAED patterns (Figure S10 in the Supporting Information). The rotation average of SAED patterns results in the relationship between the reciprocal distance and diffraction intensity (Figure 4d). The derived diffraction pattern of $Li_{0.952}Sn^{II}_{0.398}Sn^{IV}_{0.563}S_2$ can be assigned to that of $LiSnS_2$ (JCPDS No 73–1005). The broad peaks in the pattern are associated with a tiny grain size of corresponding materials, in good accordance with those revealed by TEM images. The $Na_{0.648}Sn^{II}_{0.122}Sn^{IV}_{0.777}S_2$ and $K_{0.760}Sn^{II}_{0.127}Sn^{IV}_{0.746}S_2$ also show diffraction patterns. The first diffraction ring presents at 1.26, 1.35, and 1.41 nm^{-1} for $Li_{0.952}Sn^{II}_{0.398}Sn^{IV}_{0.563}S_2$, $Na_{0.648}Sn^{II}_{0.122}Sn^{IV}_{0.777}S_2$, and $K_{0.760}Sn^{II}_{0.127}Sn^{IV}_{0.746}S_2$ (Figure 4d), respectively, which can be associated with (001) plane of samples. Accordingly, the distance of (001) planes is 0.79 nm for $Li_{0.952}Sn^{II}_{0.398}Sn^{IV}_{0.563}S_2$, 0.71 nm for $Na_{0.648}Sn^{II}_{0.122}Sn^{IV}_{0.777}S_2$, and 0.70 nm for $K_{0.760}Sn^{II}_{0.127}Sn^{IV}_{0.746}S_2$. The increase of (001) plane distance is

in good accordance with previous experimental and calculation reports.[46,47] Elemental mapping carried out in TEM (Figure S11 in the Supporting Information) shows Na, and K are distributed uniformly in corresponding samples. The atomic number of Li is too small to assess by elemental mapping.

The chemical structure of pristine SnS_2 and ion-intercalated SnS_2 was revealed by XPS. Sn 3d window of XPS spectra (Figure 4e) shows that after ion intercalation, the binding energies of Sn are negatively shifted in comparison with pristine SnS_2. The binding energy of Sn $3d_{5/2}$ is 486.4 eV for pristine SnS_2, while it shifted to 486.0 eV for $Li_{0.952}Sn^{II}_{0.398}Sn^{IV}_{0.563}S_2$, 486.1 eV for $Na_{0.648}Sn^{II}_{0.122}Sn^{IV}_{0.777}S_2$, and 486.1 eV for $K_{0.760}Sn^{II}_{0.127}Sn^{IV}_{0.746}S_2$. Sn presents as +2 to +4 valence in the intercalated samples,[52] while only +4 Sn can be found in the pristine sample. The partial reduction of Sn is associated with electron injection to compensate the charge with ion intercalation. The binding energies of S $2p_{3/2}$ are positively shifted after ion intercalation (Figure 4f), with a binding energy of 161.6 eV for SnS_2, 162.0 eV for $Li_{0.952}Sn^{II}_{0.398}Sn^{IV}_{0.563}S_2$, 161.8 eV for $Na_{0.648}Sn^{II}_{0.122}Sn^{IV}_{0.777}S_2$, and 161.8 eV for $K_{0.760}Sn^{II}_{0.127}Sn^{IV}_{0.746}S_2$. Meanwhile, no evidence of surface oxidation was found (Figure S12 in the Supporting Information), which is generally indicated by the absence of the XPS signal at a binding energy of 168.6 eV corresponding to the S—O bond. Accordingly, the oxidation of sulfide is negligible during ion intercalation and NLO measurement.

Ion-intercalation varies the number and position of defect states in the bandgap of SnS_2. The presence of in-gap defect states is implied by the linear optical absorption of photon with wavelength larger than 700 nm (Figure 1i), i.e., the absorption of photons with energy smaller than the bandgap energy (E_g) of samples (Figure S13 in the Supporting Information). Meanwhile, the ultraviolet photoelectron spectroscopy (UPS) spectra reveal the band-tail states that present in the bandgap of samples (Figure 4g). It is generally considered that the band-tail states are associated with a structural imperfection or chemical impurity.[53] For ion-intercalated SnS_2, both factors would contribute to the introduction of band tails, with Li^+, Na^+, or K^+ as a chemical impurity, and structural imperfection resulted from lattice expansion. To explicitly evidence the presence of in-gap defect states and construct the energy band model of samples, surface photovoltage (SPV) spectra were measured. SPV is correlated with the population and/or depopulation of in-gap states,[54] and has been widely utilized to characterize the in-gap defect states of semiconductor.[55–57] The SPV spectra of pristine and ion-intercalated SnS_2 are shown in panel a to d of Figure S14 in the Supporting Information. In SPV spectra the in-gap states would induce the variation of the slope of SPV versus hv.[58] According the slope variation of SPV and E_g of samples, the position of in-gap states relative to the conduction band minimum and the valence band maximum (VBM) are derived, and the energy band model are proposed in Figure S14e in the Supporting Information. A small band of in-gap states is found for the pristine SnS_2 at ≈1.72 V above the VBM, in accordance with small peak near 700 nm (1.81 eV) in the absorption spectrum of SnS_2 (Figure 1i). After ion-intercalation, more defect states are presented in the bandgap and their distribution is wider. The defects states locate in ≈0.80–1.66 eV above the VBM of $K_{0.760}Sn^{II}_{0.127}Sn^{IV}_{0.746}S_2$, 0.74–1.47 eV above the VBM of $Na_{0.648}Sn^{II}_{0.122}Sn^{IV}_{0.777}S_2$, and 0.21–1.59 eV above the VBM of $Li_{0.952}Sn^{II}_{0.398}Sn^{IV}_{0.563}S_2$. The density of states (DOS) of in-gap states was estimated from UPS spectra (Figure 4g). The VBM can be determined by the extrapolation of a line fit to the leading edge of the spectrum. The intensity of the band-tail signal is much intensive in ion-intercalated samples than SnS_2, suggesting a larger amount of defect states in the bandgap of the ion-intercalated SnS_2 than those in the pristine SnS_2.

The characterization of crystal structure and band structure of SnS_2 and ion-intercalated SnS_2 are summarized in **Figure 5**a. Figure 5a shows the *c*-axis lattice expansion of the comparative samples which was calculated by the (001) plane distance derived from SAED patterns. The bandgap of SnS_2 and ion-intercalated SnS_2 was derived from absorption spectra and shown in (Figure S13 in the Supporting Information). The E_g is 2.63 eV for SnS_2, 2.09 eV for $Li_{0.952}Sn^{II}_{0.398}Sn^{IV}_{0.563}S_2$, 2.11 eV for $Na_{0.648}Sn^{II}_{0.122}Sn^{IV}_{0.777}S_2$, and 2.27 eV for $K_{0.760}Sn^{II}_{0.127}Sn^{IV}_{0.746}S_2$ (Figure 5a). Bandgap narrowing was found for all ion-intercalated samples, with a smaller bandgap corresponding to a smaller radius of intercalating atoms. Quantitative comparison of the number of the in-gap states was accomplished by the normalized area of the band-tail signal of UPS spectra, with that of SnS_2 defined as 1. The normalized DOS of the band tail of $Li_{0.952}Sn^{II}_{0.398}Sn^{IV}_{0.563}S_2$ is ≈12.3, and it is 6.0 for $Na_{0.648}Sn^{II}_{0.122}Sn^{IV}_{0.777}S_2$, and 5.6 for $K_{0.760}Sn^{II}_{0.127}Sn^{IV}_{0.746}S_2$ (Figure 5a). It is shown that the number of the DOS of the in-gap states correlates strongly with the *c*-axis lattice expansion (alkali ion radius), a larger *c*-axis expansion (a smaller alkali ion radius) resulting in a larger number of the DOS of in-gap states.

The summaries in Figure 5a and the NLO properties shown in Figure 2 suggest that the optical nonlinearity of pristine SnS_2 and ion-intercalated SnS_2 correlates strongly with the number of in-gap states. Before the discussion of the contribution of in-gap states to optical nonlinearity, the nature of optical nonlinearity should be clarified for reverse saturable absorption. The slopes derived from the log–log plot of nonlinear absorption (ΔT_0, the depth of the valley in the Z-scan traces) and the laser-pulse energy (E) are shown in Figure 5b for samples showing revere saturable absorption, and the corresponding $\log(\Delta T_0)$–$\log(E)$ plots can be found in Figure S15 in the Supporting Information. The slope is associated with the order of optical nonlinearity, a process of nominal (n+1) photon absorption corresponding to a slope of n. It is shown that the slope is around 1 for all samples at all wavelengths except SnS_2 with the laser excitation of 1030 nm, whose slope is 1.56. It can be deduced that the combination of nominal 2PA and 3PA occurs for SnS_2 under the laser excitation at 1030 nm, while other reverse saturable absorption comes from nominal 2PA (the third-order optical nonlinearity). On the other hand, the reverse saturable absorption might come from instantaneous two- or multiple-photon absorption, or the successive excitation process (e.g., excited state absorption). To clarify to nature of reverse saturable absorption, the pump-probe experiments of SnS_2 and $Li_{0.952}Sn^{II}_{0.398}Sn^{IV}_{0.563}S_2$ were carried out with the 800 nm laser used as both the pump beam and probe beam. The decay curve of SnS_2 is symmetric (Figure 5c1), suggesting that the reverse saturable absorption in SnS_2 is an instantaneous process, namely, a pure two-photon absorption process.[59] In contrast, the decay curve is asymmetric for $Li_{0.952}Sn^{II}_{0.398}Sn^{IV}_{0.563}S_2$.

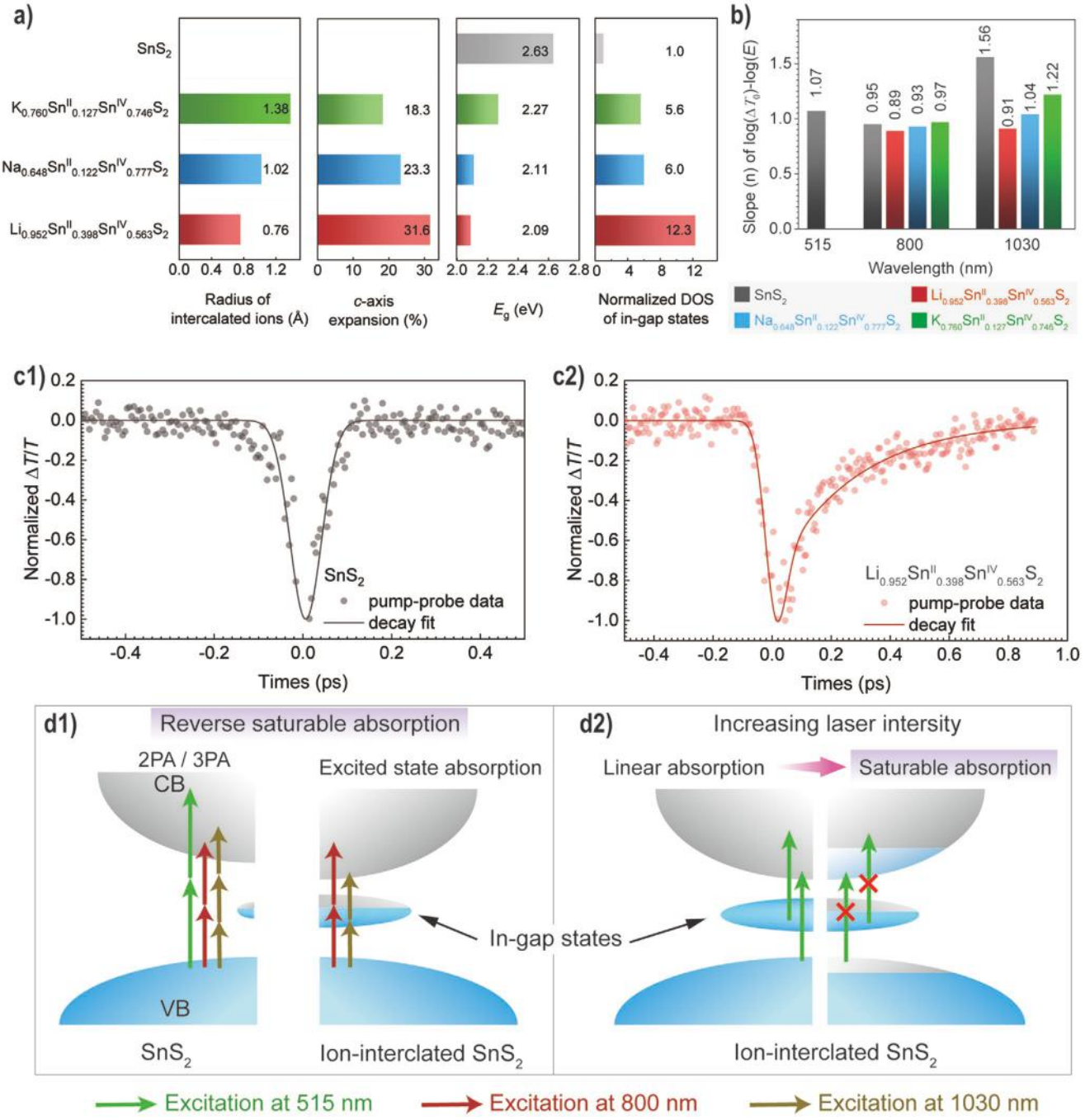

Figure 5. a) The summary of the radii of intercalated ions, the *c*-axis expansion, the E_g, and the normalized DOS of in-gap states for SnS_2 and ion-intercalated SnS_2. b) the slopes of $\log(\Delta T_0)$-$\log(E)$ plots for SnS_2 and ion-intercalated SnS_2 with the laser excitation at 515, 800, and 1030 nm. ΔT_0 is the depth of the valley in the *Z*-scan traces, and *E* is the pulse energy of excitation. c) Pump-probe curves of (c1) SnS_2 and (c2) $Li_{0.952}Sn^{II}_{0.398}Sn^{IV}_{0.563}S_2$. d) The schematic of the DOS of SnS_2 and ion-intercalated SnS_2, and corresponding excitation model for (the left panel of d1) the 2PA/3PA of pristine SnS_2, and (the right panel of d1) the excited state absorption and (d2) Pauli blocking of ion-intercalated SnS_2.

(Figure 5c2). The asymmetric trace indicates that the optical nonlinearity of $Li_{0.952}Sn^{II}_{0.398}Sn^{IV}_{0.563}S_2$ should be ascribed to a successive process, namely, excited state absorption.[59]

The excitation process and the DOS of SnS_2 and ion-intercalated SnS_2 are schematically proposed in Figure 5d. The pristine SnS_2 has an E_g of 2.63 eV, and the DOS of in-gap defect states is relatively small. Meanwhile, pump-probe experiment suggests that the reverse saturable absorption of SnS_2 is an instantaneous process. Accordingly, the NLO response can be associated with VB to CB excitation as a result of the 2PA/3PA process (Figure 5d1, left). With the laser excitation at 515 and 800 nm, the photon energy ($h\nu$) is 2.4 and 1.5 eV, respectively. The E_g satisfies $h\nu < E_g < 2h\nu$, so that 2PA occurs under these two wavelengths. The $h\nu$ is 1.2 eV for 1030 nm laser, and E_g has

a relationship $2h\nu < E_g < 3h\nu$, and accordingly 3PA is responsible for the reverse saturable absorption of pristine SnS_2 under the laser excitation of 1030 nm. Meanwhile, the in-gap states might also be excited by two photon absorption to the conduction band with the laser excitation at 1030 nm, so that two photon absorption might be possible as suggested by the slope of $\log(\Delta T_0)$–$\log(E)$ plots.

The reverse saturable absorption of ion-intercalated SnS_2 should be a successive excitation process (excited state absorption) according to the pump-probe experiment of $Li_{0.952}Sn^{II}_{0.398}Sn^{IV}_{0.563}S_2$ (Figure 5c2). With the laser excitation at 800 and 1030 nm, the photon energy ($h\nu$) is 1.5, and 1.2 eV, respectively. All photon energies are smaller than the bandgap of ion-intercalated SnS_2 (2.09–2.27 eV), so that the excited states should be referenced to in-gap states in the excited-state absorption (Figure 5d1, right). In this scenario, the larger DOS of in-gap states, the more real intermediate states are accessible during excited-state absorption, and the more pronounced reverse saturable absorption can occur. Experiments indeed confirm this relationship.

For laser excitation at 515 nm, the E_g of $Li_{0.952}Sn^{II}_{0.398}Sn^{IV}_{0.563}S_2$, $Na_{0.648}Sn^{II}_{0.122}Sn^{IV}_{0.777}S_2$, and $K_{0.760}Sn^{II}_{0.127}Sn^{IV}_{0.746}S_2$ are all smaller than the photon energy, so that one-photon absorption process would occur and result in the SA in these samples (Figure 5d2). The electrons in the valence band (VB) can absorb the energy of one photon and be excited to the conduction band (CB). With increasing incident laser intensity, the electrons would be accumulated in CB if the recombination rate of excited carriers is sufficiently slow. Accordingly, the further excitation of VB electrons would be hindered because the CB is accumulated with electrons and a Pauli-blocking effect. The absorption of the sample would decrease with increasing laser intensity. Meanwhile, the electrons occupying in-gap levels can also be excited to the CB, and would intensify the Pauli-blocking effect. Consequently, more in-gap levels in $Li_{0.952}Sn^{II}_{0.398}Sn^{IV}_{0.563}S_2$ would result in more prominent saturable absorption, in comparison with $Na_{0.648}Sn^{II}_{0.122}Sn^{IV}_{0.777}S_2$.

Figure 3b shows that the $Li_{0.952}Sn^{II}_{0.398}Sn^{IV}_{0.563}S_2$ subjected to the de-intercalation process possesses a larger reverse saturable absorption in comparison with pristine SnS_2. The UPS spectrum of de-intercalated SnS_2 (Figure S16 in the Supporting Information) indicates that the DOS of in-gap states of the de-intercalated SnS_2 are larger than that of pristine SnS_2. According to the model proposed above, more intermediate states would be available for effective excited-state absorption in de-intercalated SnS_2 than that in pristine SnS_2, and therefore a larger reverse saturable absorption can be found in de-intercalated SnS_2.

3. Conclusion

In summary, we have shown that electrochemical ion intercalation is an effective approach to realizing giant NLO response of 2D materials at different laser wavelengths. Electrochemical ion intercalation of SnS_2 nanosheets results in a superb nonlinear optical material, $Li_{0.952}Sn^{II}_{0.398}Sn^{IV}_{0.563}S_2$, whose exhibits strong saturable absorption with the laser excitation at 515 nm ($\beta_{eff} = -1.7 \times 10^4$ cm GW^{-1}) and prominent reverse saturable absorption with the laser excitation at 800 nm ($\beta_{eff} = 2.8 \times 10^4$ cm GW^{-1}) and 1030 nm ($\beta_{eff} = 1.4 \times 10^4$ cm GW^{-1}). The performance is superb to most NLO materials. Structural and spectral characterization suggest that the giant optical nonlinearity can be attributed to abundant defect states introduced by ion intercalation. Alkali-metal ion with smaller radius results in larger lattice expansion along *c*-axis and therefore a larger amount of in-gap defect states, consequently leading to better NLO properties. In-gap states can intensify the Pauli-blocking effect with the laser excitation at 515 nm, and promote the saturable absorption. On the other hand, in-gap states act as efficient intermediate states that participate in the excited state absorption in the laser excitation at 800 and 1030 nm, and are responsible for enhanced reverse saturable absorption. The repeated modulation via ion intercalation and de-intercalation was also demonstrated, and the $Li_{0.952}Sn^{II}_{0.398}Sn^{IV}_{0.563}S_2$ is stable under the ambient atmosphere for at least 8 weeks. Our results introduce a new kind of high-performance NLO materials, demonstrate an effective manner to modulate the NLO response of materials, and also broaden the knowledge concerning defect-dependent NLO response of materials.

4. Experimental Section

Materials: Stannous chloride dihydrate ($SnCl_2{\cdot}2H_2O$, AR), thioacetamide (CH_3CSNH_2, AR), ethanol (C_2H_6O, AR), acetone (C_3H_6O, AR), 2-propanol ($(CH_3)_3CHOH$, AR) were purchased from Sinopharm Chemical Reagent Co. Ltd. (Shanghai, China). Lithium hexafluorophosphate acetonitrile ($LiPF_6$/ACN, AR), sodium hexafluorophosphate acetonitrile ($NaPF_6$/ACN, AR) and potassium hexafluorophosphate acetonitrile (KPF_6/ACN, AR) were purchased from Sinopharm Chemical Reagent Co. Ltd. (Shanghai, China). All chemical reagents were used as received.

Synthesis of SnS_2 Nanosheets: The SnS_2 nanosheets were synthesized by chemical bath deposition in ambient atmosphere. Typically, $SnCl_2{\cdot}2H_2O$ (0.28 g) and thioacetamide (0.27 g) were dissolved in ethanol (200 mL) in a glass beaker to form a clear solution. Then, a piece of bare FTO substrate was horizontally immersed into the solution. The deposition was then carried out at 48 °C for 3 h. After cooling down to room temperature (≈25 °C), the FTO substrate loaded with a thin film of SnS_2 nanosheets was washed with deionized water and ethanol. Finally, the samples were dried in a vacuum at 60 °C. The O_2 dissolved in water acts as an oxidant during the reaction. The chemical reaction equation can be proposed for the synthesis carried out in ambient atmosphere:

$$CH_3NH_2C{=}S + 2CH_3CH_2OH \rightarrow CH_3(NH_2)C(OC_2H_5)_2 + H_2S \quad (1)$$

$$2SnCl_2 + 4H_2S + O_2 \rightarrow 2SnS_2 + 4HCl + 2H_2O \quad (2)$$

Assembly of the Device: The FTO substrate loaded with SnS_2 nanosheets served as the working electrode, and the electrolyte was 1 M $LiPF_6$/CAN, $NaPF_6$/CAN, or KPF_6/ACN. The electrolyte was sealed between the working electrode and a bare quartz by a hot-melting Surlyn membrane (60 μm thick). Two pieces of Pt wires were inserted into the electrolyte and act as the counter electrode and the reference electrode, respectively. All potentials are referenced to the Pt reference electrode.

The Optical Nonlinearity Measurements: Open-aperture *Z*-scan experiments was carried out using a *Z*-scan Kit from Newport. The samples were excited with laser radiation at several wavelengths, including 1030 nm (1000 Hz repetition rate, 34 fs pulse width, 300 nJ

single-pulse energy), 800 nm (1000 Hz repetition rate, 34 fs pulse width, 40 nJ single-pulse energy) and 515 nm (1000 Hz repetition rate, 34 fs pulse width, 150 nJ single-pulse energy). The pulse laser was generated by Solstice Ace (Spectra-Physics) and optical parameter amplifier (TOPAS-Prime-U, Newport). During the *Z*-scan the sample was moved along the *z*-axis of focused laser beam by the ILS250CC DC servo linear stage (Newport), and the intensity of transmittance beam was measured by photodiode sensor (918D-SL-OD3R, Newport) and optical power meter (2936-R, Newport). The Z-scan curves were fitted using the equation in ref. [60]. For process containing the third- and fifth-order optical nonlinearity, the fitting of Z-scan curves was carried out with the method introduced in Note S1 in the Supporting Information. A home-built pump-probe setup was used for the pump-probe experiment. The 800 nm laser was used as both the pump beam and the probe beam. The angle between the pump beam and probe beam was 5°. A chopper (OE3001, Sine Science Instruments) was inserted in the pump beam, and the intensity of the probe beam passed through the sample was monitored by a photodiode (PDA100A2, Thorlabs) linked to a lock-in amplifier (OE1022D, Sine Science Instruments). The delay line is a hollow retroreflector (UBBR2.5-1S, Newport) loaded on a computer-controlled travel stage (LTS300/M, Thorlabs).

Characterization: A Hitachi S-4800 was used for SEM experiments, and a Titan Cubed Themis G2 300 (FEI) for TEM experiments. XPS experiment was carried out on a Kratos Axis Ultra DLD. SPV spectra were recorded on a surface photovoltage spectrometer (CEL-SPS1000), and the extraction of defect level from SPV spectra was introduced in Note S2 in the Supporting Information. UPS experiment was performed on a photoelectron spectrometer (ESCALAB 250Xi, Thermo Fisher Scientific).

Supporting Information

Supporting Information is available from the Wiley Online Library or from the author.

Acknowledgements

M.D. and H.L. contributed equally to this work. This research was financially supported by the National Natural Science Foundation of China (51772214, 51432006), the Ministry of Science and Technology of China (2011DFG52970), the Ministry of Education of China (IRT14R23), 111 Project (B13025), the Innovation Program of Shanghai Municipal Education Commission, and the national youth talent support program (W03070073).

Conflict of Interest

The authors declare no conflict of interest.

Data Availability Statement

Research data are not shared.

Keywords

electrochemical doping, intercalation, nonlinear absorption, nonlinear optics, saturable absorption, tin disulfide

Received: July 19, 2021
Revised: August 23, 2021
Published online: September 4, 2021

[1] U. Keller, *Nature* **2003**, *424*, 831.
[2] X. Yin, Z. Ye, D. A. Chenet, Y. Ye, K. O'Brien, J. C. Hone, X. Zhang, *Science* **2014**, *344*, 488.
[3] C. Zhang, Y. Song, F. E. Kühn, Y. Wang, X. Xin, W. A. Herrmann, *Adv. Mater.* **2002**, *14*, 818.
[4] V. R. Almeida, C. A. Barrios, R. R. Panepucci, M. Lipson, *Nature* **2004**, *431*, 1081.
[5] J. Wang, Y. Hernandez, M. Lotya, J. N. Coleman, W. J. Blau, *Adv. Mater.* **2009**, *21*, 2430.
[6] Y. Xu, Z. Liu, X. Zhang, Y. Wang, J. Tian, Y. Huang, Y. Ma, X. Zhang, Y. Chen, *Adv. Mater.* **2009**, *21*, 1275.
[7] L. Wu, Y. Dong, J. Zhao, D. Ma, W. Huang, Y. Zhang, Y. Wang, X. Jiang, Y. Xiang, J. Li, Y. Feng, J. Xu, H. Zhang, *Adv. Mater.* **2019**, *31*, 1807981.
[8] L. Xu, J. Sun, T. Tang, H. Zhang, M. Sun, J. Zhang, J. Li, B. Huang, Z. Wang, Z. Xie, W.-Y. Wong, *Angew. Chem., Int. Ed.* **2021**, *60*, 11326.
[9] K. Wang, B. M. Szydłowska, G. Wang, X. Zhang, J. J. Wang, J. J. Magan, L. Zhang, J. N. Coleman, J. Wang, W. J. Blau, *ACS Nano* **2016**, *10*, 6923.
[10] Y. Xu, W. Wang, Y. Ge, H. Guo, X. Zhang, S. Chen, Y. Deng, Z. Lu, H. Zhang, *Adv. Funct. Mater.* **2017**, *27*, 1702437.
[11] C. Zhao, Y. Zou, Y. Chen, Z. Wang, S. Lu, H. Zhang, S. Wen, D. Tang, *Opt. Express* **2012**, *20*, 27888.
[12] K. Wang, J. Wang, J. Fan, M. Lotya, A. O'Neill, D. Fox, Y. Feng, X. Zhang, B. Jiang, Q. Zhao, H. Zhang, J. N. Coleman, L. Zhang, W. J. Blau, *ACS Nano* **2013**, *7*, 9260.
[13] X. Tian, H. Luo, R. Wei, C. Zhu, Q. Guo, D. Yang, F. Wang, J. Li, J. Qiu, *Adv. Mater.* **2018**, *30*, 1801021.
[14] S. Zhang, N. Dong, N. McEvoy, M. O'Brien, S. Winters, N. C. Berner, C. Yim, Y. Li, X. Zhang, Z. Chen, L. Zhang, G. S. Duesberg, J. Wang, *ACS Nano* **2015**, *9*, 7142.
[15] Y. Dong, S. Chertopalov, K. Maleski, B. Anasori, L. Hu, S. Bhattacharya, A. M. Rao, Y. Gogotsi, V. N. Mochalin, R. Podila, *Adv. Mater.* **2018**, *30*, 1705714.
[16] Y. Wang, Y. Wang, K. Chen, K. Qi, T. Xue, H. Zhang, J. He, S. Xiao, *ACS Nano* **2020**, *14*, 10492.
[17] I. Abdelwahab, P. Dichtl, G. Grinblat, K. Leng, X. Chi, I.-H. Park, M. P. Nielsen, R. F. Oulton, K. P. Loh, S. A. Maier, *Adv. Mater.* **2019**, *31*, 1902685.
[18] F. Zhou, I. Abdelwahab, K. Leng, K. P. Loh, W. Ji, *Adv. Mater.* **2019**, *31*, 1904155.
[19] H. Mu, Z. Wang, J. Yuan, S. Xiao, C. Chen, Y. Chen, Y. Chen, J. Song, Y. Wang, Y. Xue, H. Zhang, Q. Bao, *ACS Photonics* **2015**, *2*, 832.
[20] L. Zhang, J. Liu, J. Li, Z. Wang, Y. Wang, Y. Ge, W. Dong, N. Xu, T. He, H. Zhang, W. Zhang, *Laser Photonics Rev.* **2020**, *14*, 1900409.
[21] M. Diao, H. Li, R. Hou, Y. Liang, J. Wang, Z. Luo, Z. Huang, C. Zhang, *ACS Appl. Mater. Interfaces* **2020**, *12*, 7423.
[22] Y. Xu, X.-F. Jiang, Y. Ge, Z. Guo, Z. Zeng, Q.-H. Xu, H. Zhang, X.-F. Yu, D. Fan, *J. Mater. Chem. C* **2017**, *5*, 3007.
[23] Y. Ge, S. Chen, Y. Xu, Z. He, Z. Liang, Y. Chen, Y. Song, D. Fan, K. Zhang, H. Zhang, *J. Mater. Chem. C* **2017**, *5*, 6129.
[24] M. Currie, J. D. Caldwell, F. J. Bezares, J. Robinson, T. Anderson, H. Chun, M. Tadjer, *Appl. Phys. Lett.* **2011**, *99*, 211909.
[25] G. S. Painter, D. E. Ellis, *Phys. Rev. B* **1970**, *1*, 4747.
[26] S. P. Koenig, R. A. Doganov, H. Schmidt, A. H. Castro Neto, B. Özyilmaz, *Appl. Phys. Lett.* **2014**, *104*, 103106.
[27] Z. Cheng, J. Lin, *CrystEngComm* **2010**, *12*, 2646.
[28] X. Dai, X. Zhang, I. M. Kislyakov, L. Wang, J. Huang, S. Zhang, N. Dong, J. Wang, *Opt. Express* **2019**, *27*, 13744.
[29] X. Jiang, S. Liu, W. Liang, S. Luo, Z. He, Y. Ge, H. Wang, R. Cao, F. Zhang, Q. Wen, J. Li, Q. Bao, D. Fan, H. Zhang, *Laser Photonics Rev.* **2018**, *12*, 1700229.
[30] G. Wang, D. Bennett, C. Zhang, C. Ó. Coileáin, M. Liang, N. McEvoy, J. J. Wang, J. Wang, K. Wang, V. Nicolosi, W. J. Blau, *Adv. Opt. Mater.* **2020**, *8*, 1902021.

[31] M. Z. Alam, I. de Leon, R. W. Boyd, *Science* **2016**, *352*, 795.
[32] J. Huang, N. Dong, N. McEvoy, L. Wang, C. Ó. Coileáin, H. Wang, C. P. Cullen, C. Chen, S. Zhang, L. Zhang, J. Wang, *ACS Nano* **2019**, *13*, 13390.
[33] K.-G. Zhou, M. Zhao, M.-J. Chang, Q. Wang, X.-Z. Wu, Y. Song, H.-L. Zhang, *Small* **2015**, *11*, 694.
[34] J. Zhang, A. Yang, X. Wu, J. van de Groep, P. Tang, S. Li, B. Liu, F. Shi, J. Wan, Q. Li, Y. Sun, Z. Lu, X. Zheng, G. Zhou, C.-L. Wu, S.-C. Zhang, M. L. Brongersma, J. Li, Y. Cui, *Nat. Commun.* **2018**, *9*, 5289.
[35] M. S. Stark, K. L. Kuntz, S. J. Martens, S. C. Warren, *Adv. Mater.* **2019**, *31*, 1808213.
[36] J. Xu, J. Ma, Q. Fan, S. Guo, S. Dou, *Adv. Mater.* **2017**, *29*, 1606454.
[37] C. Yuan, H. B. Wu, Y. Xie, X. W. D. Lou, *Angew. Chem., Int. Ed.* **2014**, *53*, 1488.
[38] Q. Yun, Q. Lu, X. Zhang, C. Tan, H. Zhang, *Angew. Chem., Int. Ed.* **2018**, *57*, 626.
[39] W. Shi, M. Gao, J. Wei, J. Gao, C. Fan, E. Ashalley, H. Li, Z. Wang, *Adv. Sci.* **2018**, *5*, 1700602.
[40] E. J. Fuller, F. E. Gabaly, F. Léonard, S. Agarwal, S. J. Plimpton, R. B. Jacobs-Gedrim, C. D. James, M. J. Marinella, A. A. Talin, *Adv. Mater.* **2017**, *29*, 1604310.
[41] T. P. Ying, M. X. Wang, X. X. Wu, Z. Y. Zhao, Z. Z. Zhang, B. Q. Song, Y. C. Li, B. Lei, Q. Li, Y. Yu, E. J. Cheng, Z. H. An, Y. Zhang, X. Y. Jia, W. Yang, X. H. Chen, S. Y. Li, *Phys. Rev. Lett.* **2018**, *121*, 207003.
[42] J. S. Kang, M. Ke, Y. Hu, *Nano Lett.* **2017**, *17*, 1431.
[43] Y. Deng, Y. Yu, Y. Song, J. Zhang, N. Z. Wang, Z. Sun, Y. Yi, Y. Z. Wu, S. Wu, J. Zhu, J. Wang, X. H. Chen, Y. Zhang, *Nature* **2018**, *563*, 94.
[44] Y. Xiao, S. H. Lee, Y.-K. Sun, *Adv. Energy Mater.* **2017**, *7*, 1601329.
[45] G. Su, V. G. Hadjiev, P. E. Loya, J. Zhang, S. Lei, S. Maharjan, P. Dong, P. M. Ajayan, J. Lou, H. Peng, *Nano Lett.* **2015**, *15*, 506.
[46] L. A. Burton, D. Colombara, R. D. Abellon, F. C. Grozema, L. M. Peter, T. J. Savenije, G. Dennler, A. Walsh, *Chem. Mater.* **2013**, *25*, 4908.
[47] D. De, J. Manongdo, S. See, V. Zhang, A. Guloy, H. Peng, *Nanotechnology* **2013**, *24*, 025202.
[48] P. Gao, L. Wang, Y.-Y. Zhang, Y. Huang, L. Liao, P. Sutter, K. Liu, D. Yu, E.-G. Wang, *Nano Lett.* **2016**, *16*, 5582.
[49] R. L. David, *CRC Handbook of Chemistry and Physics: Properties of Solids*, CRC Press, Boca Raton, FL **2005**.
[50] M. Diao, H. Li, Y. Sun, Y. Liang, Z. Yu, D. W. Boukhvalov, Z. Huang, C. Zhang, *ACS Appl. Mater. Interfaces* **2021**, *13*, 4211.
[51] Z.-B. Liu, J.-G. Tian, Z. Guo, D.-M. Ren, F. Du, J.-Y. Zheng, Y.-S. Chen, *Adv. Mater.* **2008**, *20*, 511.
[52] T. S. Reddy, M. C. Santhosh Kumar, S. Shaji, *Mater. Res. Express* **2017**, *4*, 046404.
[53] M. Kim, S. Park, J. Jeong, D. Shin, J. Kim, S. H. Ryu, K. S. Kim, H. Lee, Y. Yi, *J. Phys. Chem. Lett.* **2016**, *7*, 2856.
[54] L. Kronik, Y. Shapira, *Surf. Sci. Rep.* **1999**, *37*, 1.
[55] F. Tan, M. I. Saidaminov, H. Tan, J. Z. Fan, Y. Wang, S. Yue, X. Wang, Z. Shen, S. Li, J. Kim, Y. Gao, G. Yue, R. Liu, Z. Huang, C. Dong, X. Hu, W. Zhang, Z. Wang, S. Qu, Z. Wang, E. H. Sargent, *Adv. Funct. Mater.* **2020**, *30*, 2005155.
[56] Z. Zhao, R. V. Goncalves, S. K. Barman, E. J. Willard, E. Byle, R. Perry, Z. Wu, M. N. Huda, A. J. Moulé, F. E. Osterloh, *Energy Environ. Sci.* **2019**, *12*, 1385.
[57] I. Levine, O. G. Vera, M. Kulbak, D.-R. Ceratti, C. Rehermann, J. A. Márquez, S. Levcenko, T. Unold, G. Hodes, I. Balberg, D. Cahen, T. Dittrich, *ACS Energy Lett.* **2019**, *4*, 1150.
[58] Y. Lubianiker, I. Balberg, E. Fefer, Y. Shapira, *J. Non-Cryst. Solids* **1996**, *198–200*, 309.
[59] J. K. Zaręba, J. Szeremeta, M. Waszkielewicz, M. Nyk, M. Samoć, *Inorg. Chem.* **2016**, *55*, 9501.
[60] M. Sheik-Bahae, A. A. Said, T.-H. Wei, D. J. Hagan, E. W. van Stryland, *IEEE J. Quantum Electron.* **1990**, *26*, 760.